Instability of liquid crystal elastomers

2016 Smart Mater. Struct. 25 015016

(http://iopscience.iop.org/0964-1726/25/1/015016)

IOP Publishing Smart Materials and Structures
Smart Mater. Struct. **25** (2016) 015016 (8pp) doi:10.1088/0964-1726/25/1/015016

Instability of liquid crystal elastomers

Ning An[1], **Meie Li**[2] **and Jinxiong Zhou**[1]

[1] State Key Laboratory for Strength and Vibration of Mechanical Structures and School of Aerospace, Xi'an Jiaotong University, Xi'an 710049, People's Republic of China
[2] State Key Laboratory for Mechanical Behavior of Materials, School of Materials Science and Engineering, Xi'an Jiaotong University, Xi'an 710049, People's Republic of China

E-mail: limeie@mail.xjtu.edu.cn

Received 7 July 2015, revised 14 October 2015
Accepted for publication 4 November 2015
Published 2 December 2015

Abstract

Nematic liquid crystal elastomers (LCEs) contract in the director direction but expand in other directions, perpendicular to the director, when heated. If the expansion of an LCE is constrained, compressive stress builds up in the LCE, and it wrinkles or buckles to release the stored elastic energy. Although the instability of soft materials is ubiquitous, the mechanism and programmable modulation of LCE instability has not yet been fully explored. We describe a finite element method (FEM) scheme to model the inhomogeneous deformation and instability of LCEs. A constrained LCE beam working as a valve for microfluidic flow, and a piece of LCE laminated with a nanoscale poly(styrene) (PS) film are analyzed in detail. The former uses the buckling of the LCE beam to occlude the microfluidic channel, while the latter utilizes wrinkling or buckling to measure the mechanical properties of hard film or to realize self-folding. Through rigorous instability analysis, we predict the critical conditions for the onset of instability, the wavelength and amplitude evolution of instability, and the instability patterns. The FEM results are found to correlate well with analytical results and reported experiments. These efforts shed light on the understanding and exploitation of the instabilities of LCEs.

Keywords: liquid crystal elastomers, instability, buckling, wrinkling, finite element method

(Some figures may appear in colour only in the online journal)

1. Introduction

Liquid crystal elastomers (LCEs) combine the anisotropy of rod-like liquid crystal molecules and the stretchability of long-chain polymers, resulting in soft materials with unique features such as a large actuation stroke of ~400% [1], and large actuation stress of ~300 kPa [2]. LCEs can be classified into thermotropic and lyotropic elastomers. The simplest and the most commonly studied thermotropic LCEs are called nematic elastomers. When heated above the nematic–isotropic transition temperature, T_{NI}, the nematic LCE undergoes a phase transition and anisotropic deformation, contracting along the direction of the nematic director but expanding in the other two directions, perpendicular to the director. This coupling of orientational order and mechanical deformation has been exploited for a wide spectrum of applications, ranging from soft actuators [3–11], motors [12, 13], tunable optical and tactile devices [14–16], microfluidic valves [17], and artificial muscles [18–20], to artificial heliotropism [21].

A piece of LCE undergoes homogeneous deformation and attains a stress-free state when it is not constrained and fully deformed. This is only meaningful for material synthesis and characterization. A variety of LCE-based devices, on the other hand, integrate an LCE with other hard materials, and the deformation of the LCE is constrained. Inhomogeneous deformation and sometimes instability are associated with the constrained deformation of LCEs. For some applications such as optical devices, the wrinkling of the LCE is a nuisance and should be avoided through careful design considerations [14–16]. The instability of LCEs, on the other hand, can be exploited to design and fabricate novel devices.

Sánchez-Ferrer *et al* successfully integrated a long strip of side-chain LCE into a silicon-based microfluidic device [17]. The longitudinal direction of the LCE strip is perpendicular to the director, and the longitudinal expansion of the LCE is constrained by its surroundings. Upon heating, compressive stress builds up within the LCE, and above a critical temperature the constrained LCE strip buckles abruptly and

comes into contact with the channel walls. The fluid flow in the microfluidic channel is thus occluded. This is the first demonstration of buckled LCE being used as a microvalve for microfluidic flow control. Agrawal *et al* constrained the deformation of LCEs by laminating a thin layer of poly (styrene) (PS) on top of an LCE, giving rise to an LCE–PS bilayer that can reversibly form regular wrinkling or buckling patterns [22, 23]. For thin PS film, regular wrinkling is favored, while for thick PS film, buckling of the bilayer is preferred to attain an energy minimum state.

Motivated by these interesting and diverse instability phenomena, we present in this paper a numerical strategy to model the nonlinear deformation of LCEs, with particular emphasis on understanding its instability. Our simulation was implemented using a widely available commercial finite element software, ABAQUS, which facilitates the interaction between industry and academia. Although buckling of the LCE–PS bilayer was also simulated by Agrawal *et al* using COMSOL [23], its limitation with regards to large deformation, contact, and post-buckling is well known [24], and as such, it is not well-suited to the instability analysis of LCEs. Our efforts aid the design and optimization of complex three-dimensional LCE devices.

2. Methodology

The LCE we focus on herein is the nematic side-chain LCE, which can be synthesized by a two-step crosslinking procedure by mixing 4-methoxyphenyl 4-(but-3-en-l-yloxy) benzoate (side-chain mesogen), 1, 4-bis(undec-10-en-l-yloxy) benzene (crosslinker), and poly(methylhydrosiloxane) (polymer, PMHS) together and using a spin-casting technique [4, 5, 17]. This type of LCE is commonly used for research into monodomain LCEs, and many experimental data have accumulated in the literature [4, 5, 13, 17, 21–23]. One of the key properties of this LCE is its so-called thermoelastic curve. As shown in figure 1(a), a piece of a cuboid LCE with dimensions $L_x \times L_y \times L_z$ at temperature T is in the nematic state, with the z-axis along the director direction. Heating the elastomer above L_z^{iso}, the length along the direction of the director contracts to L_z^{iso}, while the lengths along the x and y directions expand to L_x^{iso} and L_y^{iso}, respectively. Defining the three stretches as $\lambda_x = L_x/L_x^{\mathrm{iso}}$, $\lambda_y = L_y/L_y^{\mathrm{iso}}$, and $\lambda_z = L_z/L_z^{\mathrm{iso}}$, many reported experimental data suggest that the variation of $\lambda_z(T)$ can be described by the following relation [25–27],

$$\lambda_z(T) = L_z(T)/L_z^{\mathrm{iso}} = 1 + \beta\left(1 - T/T_{\mathrm{NI}}\right)^{\alpha}. \qquad (1)$$

For the LCE considered here, fitting to experiment yields $\alpha = 0.26$, $\beta = 0.5$, and $T_{\mathrm{NI}} = 80.5\,^{\circ}\mathrm{C}$. In a real simulation, we only use equation (1) for the case $T \leqslant T_{\mathrm{NI}}$. For $T > T_{\mathrm{NI}}$, λ_z takes a constant 1 regardless of the temperature. This causes a discrepancy in the temperature near the critical transition temperature, as seen from figure 1(b). The elastomer behaves as ideally incompressible such that the deformations along the directions perpendicular to the director are dictated by $\lambda_x\lambda_y\lambda_z = 1$ with $\lambda_x = \lambda_y$.

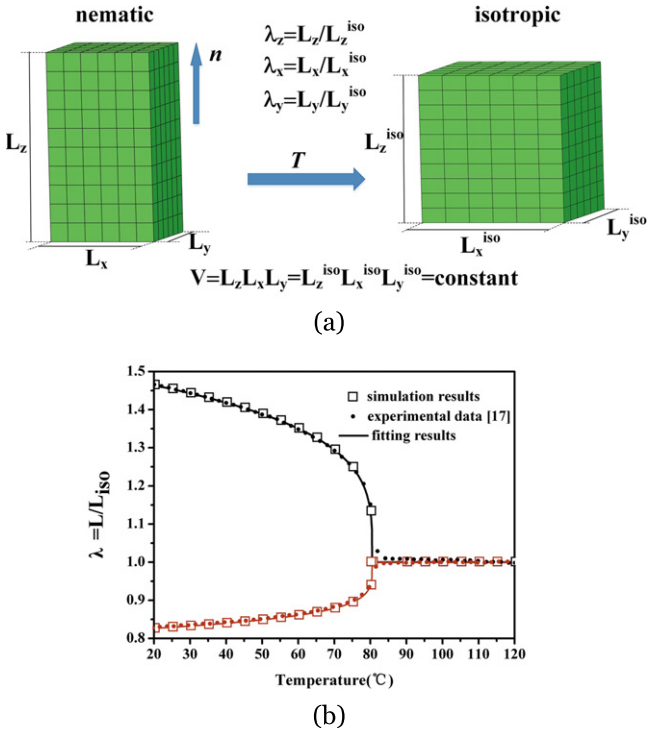

Figure 1. Anisotropic deformation and nematic–isotropic transition of a nematic elastomer. (a) Finite element method (FEM) mesh for simulation of the deformation of a nematic cuboid. The elastomer in the original nematic state of dimensions $L_x \times L_y \times L_z$ is heated and transformed into an isotropic state. The elastomer deforms anisotropically and takes dimensions $L_x^{\mathrm{iso}} \times L_y^{\mathrm{iso}} \times L_z^{\mathrm{iso}}$, contracting along the direction of the director marked by **n** but elongating along the two directions perpendicular to the director. Three stretches, λ_x, λ_y, and λ_z, are defined and the elastomer is assumed to be incompressible such that $\lambda_x\lambda_y\lambda_z = 1$. (b) Comparison of deformation versus temperature obtained by FEM simulation, experimental data reported in [17], and the fitting results. The phase transition temperature is identified as 80.5 °C. The dots are experimental data, the open squares are FEM results, and the solid lines (black and red lines for λ_z and λ_x, respectively) represent the fitting results obtained by equation (1).

The core of the simulation methodology is to implement the anisotropic stretches described by equation (1) and the incompressibility constraint into a commercial finite element software, ABAQUS, via a user-subroutine, UEXPAN. Figure 1(a) shows the element cuboid for FEM analysis, and figure 1(b) plots the comparison of the FEM result with the experimental result and its approximation by equation (1). The simulated deformations along and normal to the director fall exactly on the curves predicted by equation (1), which validates the correctness of the UEXPAN subroutine. With this, we can explore the power of FEM software to model various instability phenomena of interest in this paper.

3. Buckling of the LCE microvalve

The LCE microvalve considered here is taken from that reported by Sánchez-Ferrer *et al* [17]. Due to symmetry, only

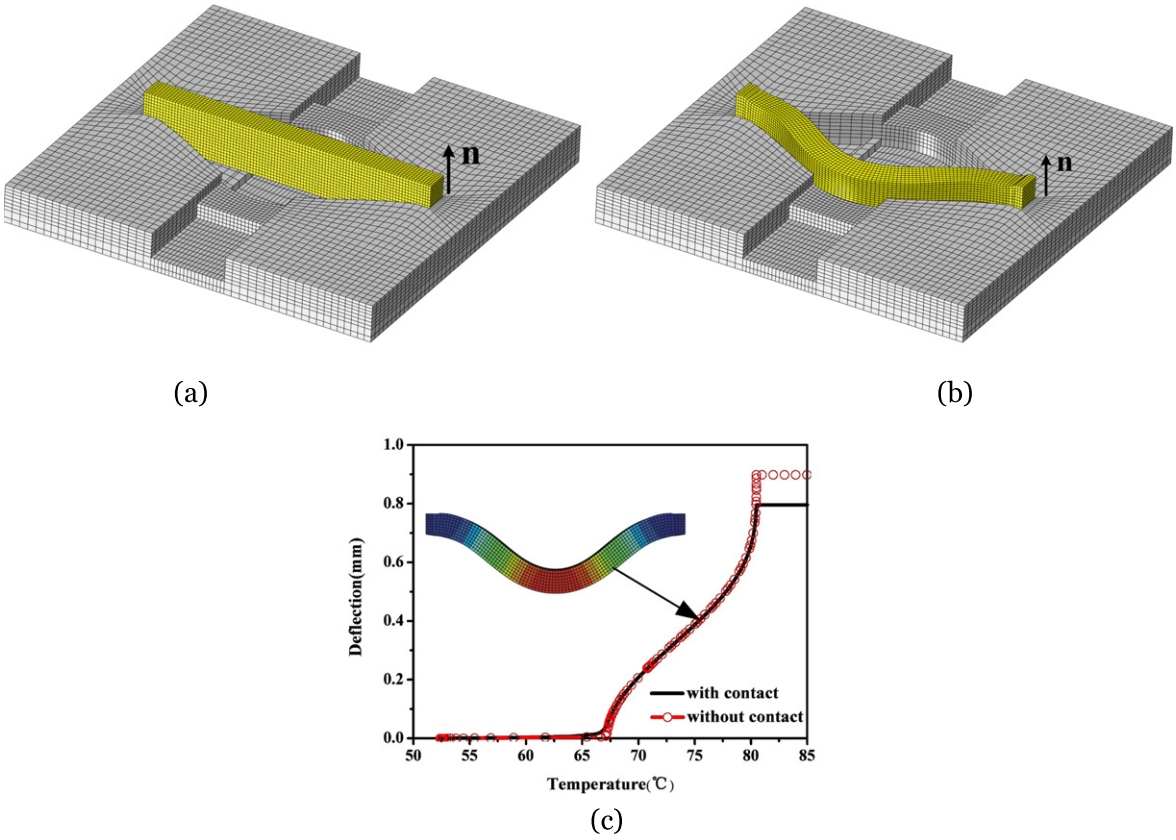

Figure 2. A microfluidic microvalve utilizes the buckling of an LCE beam to occlude the channel. (a) Reference state (52.4 °C) and (b) buckled state (80.5 °C) of the LCE-silicon microvalve. Due to symmetry, only half of the microvalve and its surroundings are modeled. (c) The deflection curve of the central point on the LCE beam obtained by a post-buckling analysis for two cases with and without contacts. The critical temperature for the onset of buckling is recognized as ~67 °C.

half of the LCE valve and the silicon channel walls are modeled in a three-dimensional (3D) model, shown in figure 2(a). The dimensions of the LCE-silicon microfluidic system are $5 \times 5 \times 1\,\text{mm}^3$, with a channel size of $1 \times 0.66\,\text{mm}^2$. The central body is a piece of LCE beam of length 3.9 mm(L_x), width 0.3 mm(L_y), and height 0.63 mm (L_z), taking an initial nematic state with **n** as the orientation of director along the z-direction. The LCE material is assumed to be linear isotropic with a Young's modulus of 60 kPa and a Poisson's ratio of 0.5 taken from [17]. Note from figure 1(b) that the dimensions of the LCE remain unchanged when the temperature is above T_{NI}. To reproduce the experimental conditions, we model the deformation of the LCE microvalve from 52.4 °C (T_{ref}) to 80.5 °C(T_{NI}). Figures 2(a) and (b) show the simulation of the reference state and the final buckled state at T_{NI}. Large deformation is considered in the simulation.

Given the specific dimensions of an LCE and the initial conditions as prepared, several key issues of primary interest for the design and application of the microvalve need to be addressed. The first issue is the critical temperature for the onset of buckling instability. We elucidate this point from different perspectives. Firstly, we estimate analytically the critical buckling temperature by using the classic Euler buckling theory [28], which gives approximately 66.1 °C. Then we perform a post-buckling analysis and plot the deflection of the central point on the beam presented in figure 2(c). The first eigenmode obtained from linear buckling analysis is used as an initial geometric imperfection for the post-buckling analysis. We identify from the linear buckling analysis and also from the central deflection curve, figure 2(c), that the critical temperatures for the onset of buckling instability are approximately 66.6 °C and 67.0 °C, respectively, both in good agreement with analytical prediction. The necessity of performing a post-buckling analysis lies in the fact that it can not only reveal the critical buckling temperature, but also predict the real deflection of the beam and detect the contact of the beam with the silicon wall for various temperatures, which is crucial for the use of the microvalve.

The second issue, from the view-point of real applications, is how large can the stress generated in the constrained LCE beam be, and how about the contact pressure between the LCE and the silicon wall? Internal stress and contact pressure that is too great would lead to the failure of the LCE, while the LCE will fail to block the flow of fluid if the contact pressure between the vale and wall is too small [29]. To answer these questions, we present in figures 3(a)–(d) the local stress distribution of the LCE vale for various temperatures, and in figure 3(e) the contact pressure between the valve and the contact surface. Note from figures 2(c) and 3 that the buckling deflection of the LCE increases steeply when the temperature approaches T_{NI}, and contact also occurs

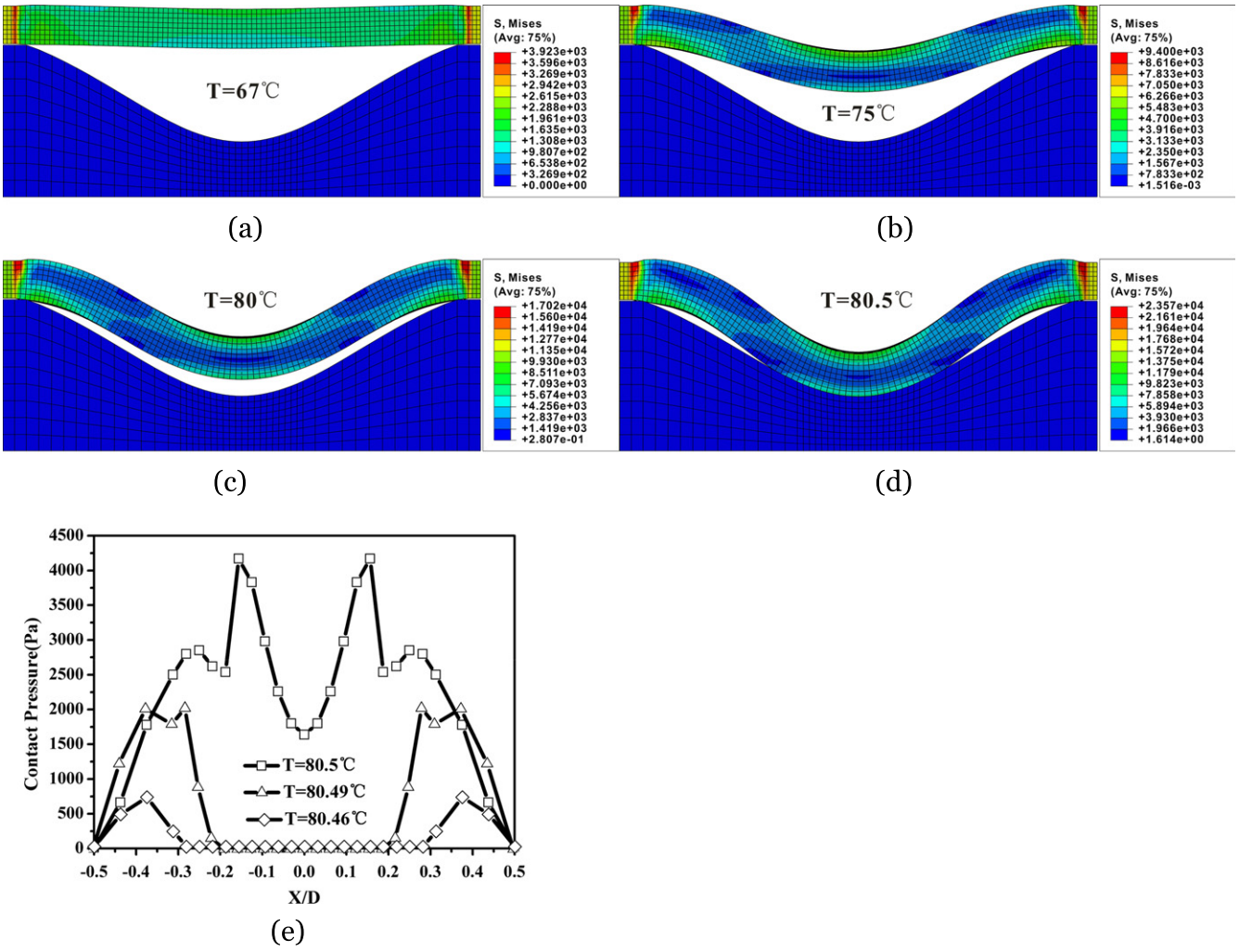

Figure 3. Local enlarged view of the deformation, stress distribution, and associated contact pressure of the LCE microvalve. (a)–(d) Deformation and stress distribution of the LCE valve for various temperatures. (e) Contact area and contact pressure between the LCE valve and the silicon wall when the temperature approaches phase transition temperature. Here X is the distance measured from the centroid of the contact and normalized by D, the length of the contact region of the LCE beam.

near this temperature for the LCE vale design modeled herein. Figure 3(c) plots the variation of the contact region as well as the contact pressure, where X is the distance measured from the centroid of the contact and normalized by D, the length of the contact region of the LCE beam. The contact pressure can also be regarded as an indicator for the state of contact: contact occurs if contact pressure is nonzero and vice versa.

4. Wrinkling and buckling of LCE–PS bilayer

Another way to constrain the deformation of an LCE is to laminate a thin layer of hard film on top of the LCE, giving rise to a bilayer as shown in figure 4. The gray substrate in figure 4 is the LCE with the director indicated by **n**, and the blue film is, for example, the PS film in experiments [22, 23]. Heating the LCE causes contraction along the direction of the director, and thus generates in-plane compressive stress in the PS film. Beyond a critical compressive stress, the LCE–PS bilayer system loses its stability and the bilayer may wrinkle or buckle to release the energy stored in the system. The different instability scenarios of the bilayer depend on the PS film thickness: for thin PS film, the bilayer wrinkles; for thick PS film, the bilayer buckles.

We present in figure 5 the wrinkling instability of the LCE coated with thin PS film ($\leqslant$400 nm in accordance with experiments). The thickness of the LCE is fixed at 0.36 mm, while the thickness of the PS film is varied from 100 nm, 200 nm, 300 nm, to 400 nm. The LCE substrate and thin PS film are assumed to be linear elastic solids with no slipping at the bilayer interface. To be specific, we set the Young's modulus and Poisson ratio for the LCE substrate and PS film to be $E_s = 0.24$ MPa, $\nu_s = 0.5$, and $E_f = 32.5$ GPa, $\nu_f = 0.32$, respectively.

For the wrinkling analysis of a film/substrate system with a large substrate/film thickness ratio, H/h of nearly 1000 for the thickest film (400 nm PS film), the thickness of the substrate (0.36 mm) can be regarded as infinite compared to that of thin film. It is unnecessary in a real simulation to model the real substrate thickness, i.e., 0.36 mm; instead, only

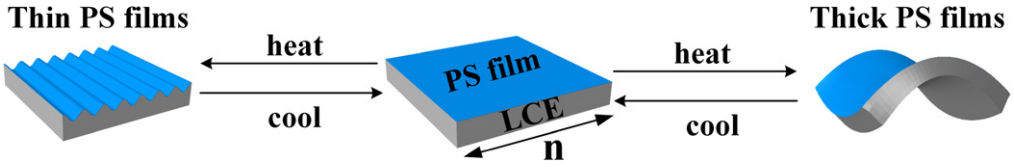

Figure 4. Schematic illustration of two deformation scenarios of an LCE–PS bilayer. If heated, the bilayer wrinkles for thin PS film but buckles for thick PS film. The transition from the wrinkled or buckled state to the flat state is reversible by cooling or heating the bilayer.

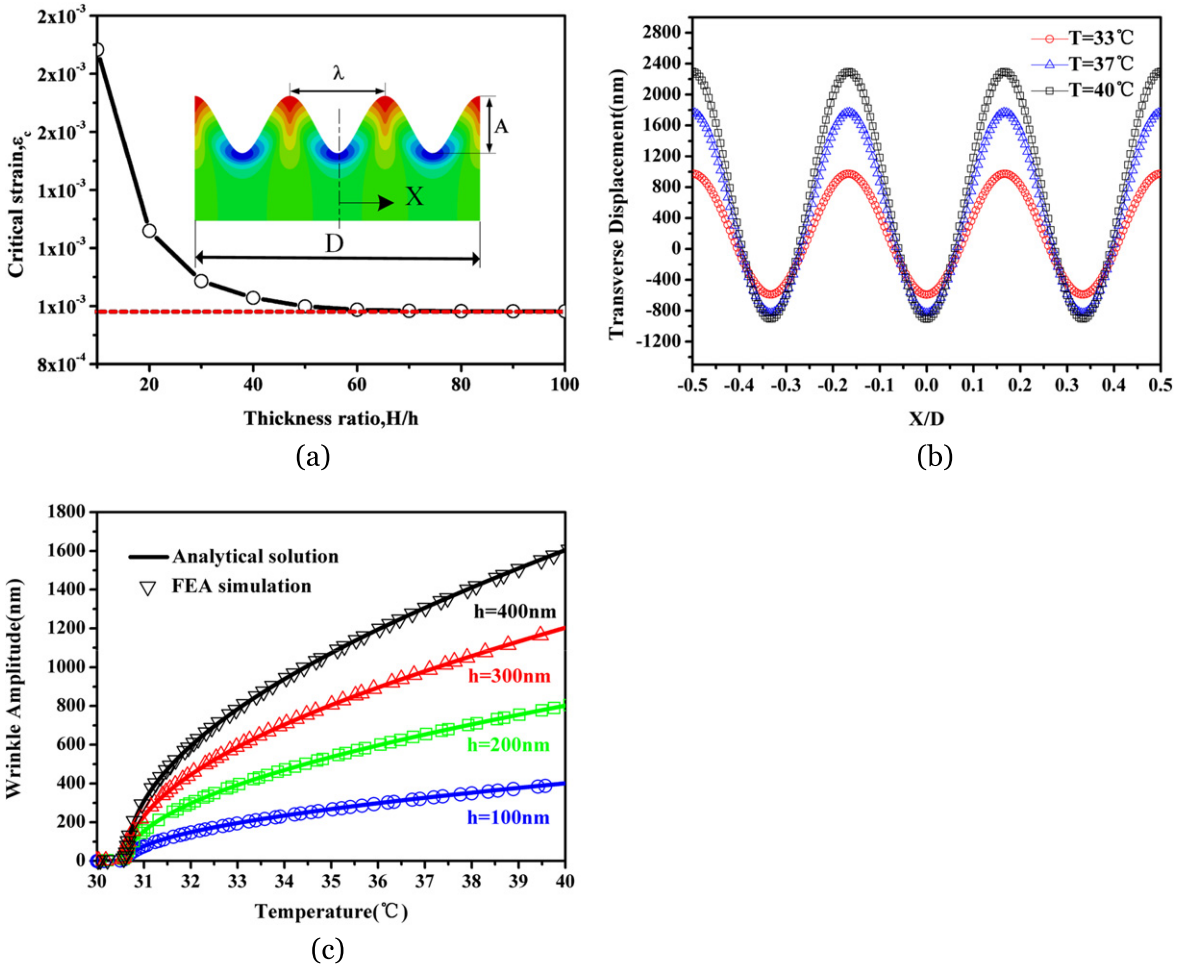

Figure 5. (a) Effects of substrate/film thickness ratio on the critical strain for the wrinkling of the system. Inserted is the simulated local wrinkling pattern for film thickness $h = 400$ nm with wavelength 0.04 mm. The horizontal dashed line is the analytical solution for an infinitely thick substrate. (b) Wrinkling profile of an LCE–PS bilayer with film thickness $h = 400$ nm for various temperatures. Heated from a reference temperature, 30 °C, the amplitude increases with increasing temperature while the wave number remains constant for the variation of temperature. (c) Comparison of simulated amplitudes with the analytical prediction. Solid lines are analytical results and markers are FEM results.

a thin layer of substrate with a thickness many times that of the film thickness, is meshed. Figure 5(a) plots the variation in critical strain for the wrinkling of the bilayer on the substrate/film thickness ratio, H/h. The red dashed line is the critical strain obtained from an analytical expression for an infinitely thick substrate [30]:

$$\varepsilon_c = \frac{1}{4}\left(\frac{3E_s}{E_f}\right)^{2/3}, \qquad (2)$$

where E_s and E_f are moduli of substrate and film, respectively. Note that the critical strain levels off when the substrate/film thickness ratio is greater than 80. We, therefore set $H/h = 100$ and perform a 2D plane-strain simulation. This treatment saves tremendous computation cost and facilitates wrinkling analysis with good accuracy, which is also adopted in the wrinkling analysis of other film/substrate systems [31]. Inserted in figure 5(a) is the wrinkling pattern of an LCE–PS bilayer with PS film thickness $h = 400$ nm. Figure 5(b) plots the wrinkling profiles for various temperatures calculated with respect to a reference temperature, 30 °C. Figure 5(b) implies that as temperature variation increases, the amplitude of wrinkling increases, too, but the wavelength remains unchanged. To simulate the wrinkle growth beyond the

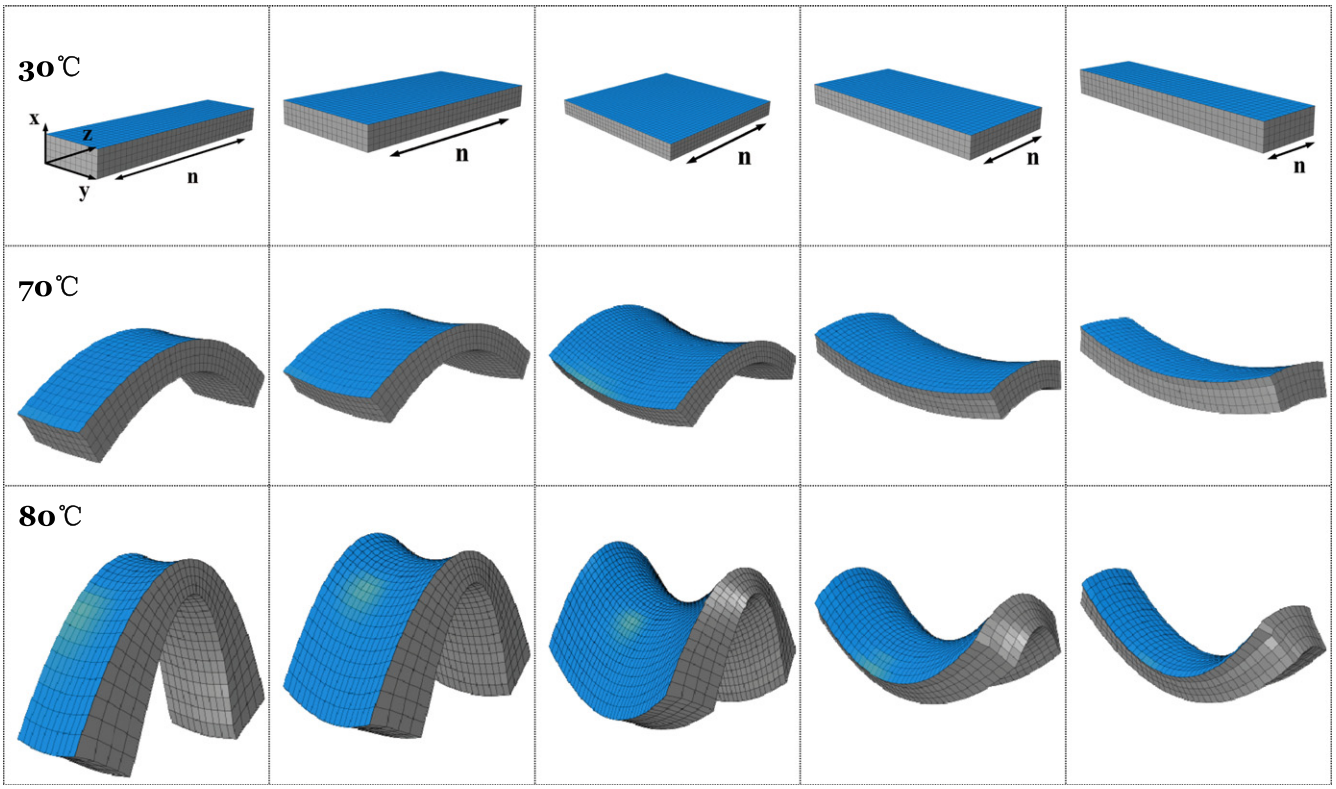

Figure 6. Buckling phase diagram of LCE–PS bilayers with various aspect ratios when temperature is varied from a reference of 30 °C (first row) to 70 °C (second row), and to 80 °C (third row), respectively. Samples in the same column have the same aspect ratio, as shown at the bottom of each column. The LCE thickness is 0.36 mm and that of the PS film is 986 nm for all models.

critical temperature, a nonlinear post-buckling analysis is performed with the 2D finite element model. The critical eigenmode obtained from the linear analysis scaled by a very small factor ($A_0/h = 2.5 \times 10^{-3}$) is introduced as a geometric imperfection to trigger the wrinkling instability. Figure 5(c) gives the variation of wrinkling amplitudes versus temperature obtained from post-buckling analysis. The solid lines are the following analytical result [30] for wrinkling amplitude corresponding to a specific wavelength, λ,

$$A(\lambda) = \lambda/\pi\sqrt{\varepsilon - \varepsilon_c}, \tag{3}$$

where ε is the strain associated with temperature that is derived from equation (1).

The unique feature of the LCE–film bilayer system is that it enables the reversible orientation of wrinkles in a single sample [22]. It may generate wrinkles either parallel or perpendicular to the nematic director. It provides a scheme to measure the mechanical properties of thin film by using the winkling instability [32]. Once the wavelength of the wrinkling, λ, is measured, the Young's modulus of the film, E_f, can be extracted from the following equation [32],

$$\lambda = 2\pi h\left(\bar{E}_f/\bar{E}_s\right)^{1/3}, \tag{4}$$

where $\bar{E}_f = E_f/(1 - \nu_f^2)$ and $\bar{E}_s = E_s/(1 - \nu_s^2)$ are the plane-strain modulus of film and substrate, respectively.

Surface wrinkling is ubiquitous in bilayer systems where a stiff, thin film is laminated on top of a soft and thick substrate. Through wrinkling, the system releases the compressive elastic energy of the system [33]. The total energy stored in the system consists of the elastic energy of substrate and the elastic energy of film, mainly bending energy if instability occurs, which is proportional to the so-called flexural rigidity, $D = \frac{E_f h^3}{12(1-\nu_f^2)}$. In the case of thin film, the bending energy of the film is small compared to the elastic energy of the substrate. Soft substrate in compression favors short wavelength wrinkling, and the film wrinkles too, to conform to the irregular surface. When the film thickness is increased, the bending energy of the film increases as a cubic law. There is a critical thickness that the bending energy of the film becomes dominant in the total energy of the system. Beyond this critical thickness, buckling or folding of the system with a long wavelength is preferred [34]. Figure 6 presents the buckling phase diagram of an LCE–PS bilayer with a 986 nm PS film. The thickness of the LCE is fixed at 0.36 mm but its aspect ratio is varied. As the temperature is raised from the reference of 30 °C (first row) to 70 °C (second row), and then 80 °C (third row), saddle-shaped buckling is observed. The transition of the curvature from convex to concave is captured. The simulated buckling patterns are in good agreement with those found experimentally and reported in the literature [23].

5. Concluding remarks

Soft and stimulus-responsive LCE couples orientational order with elastic deformation, offering unique solutions for diverse applications. In real applications, an LCE is commonly integrated with other hard materials and its deformation is constrained and inhomogeneous. LCEs are amenable to instability due to their low modulus. The instability of LCEs, however, can be exploited to design and fabricate novel devices. We implement the thermoelastic curve of the LCE into a commercial software, ABAQUS, and present a simulation scheme to model the instability of the LCE. The buckling of an LCE microvalve for microfluidic flow control and the wrinkling of an LCE–PS bilayer are analyzed for the very first time. The success of the simulation scheme and its accuracy depends on a phenomenological constitutive law adopted herein. For most of the monodomain LCEs synthesized by the two-step method, the discrepancy between the simulation and the experimental data is pretty small and is negligible. For other LCEs, the specific constitutive law should be modified accordingly, but the scheme is generic and still works provided a phenomenological approximation is available.

The power of ABAQUS's nonlinear analysis is utilized to convey some key messages from the viewpoint of applications. For the buckling of the LCE microvalve, the critical temperature for the onset of buckling, the contact state of the LCE with microfluidic channel walls, the stress distribution and the contact pressure of the LCE are predicted. For an LCE–PS bilayer and when the PS film is thin, short wavelength wrinkling instability is energy minimum, and we present the wavelength and amplitude evolution at various working temperatures. The bilayer system transits to long wavelength buckling if the PS film is beyond a critical thickness. We establish the buckling phase diagram for various aspect ratios and temperatures. All these instability analyses are in good agreement with analytical results and reported experimental results. Our efforts shed light on the understanding, programmable modulation, and utilization of various instabilities of LCEs, and will aid the design and development of LCE-based soft devices.

Acknowledgments

This research is supported by Natural Science Foundation of China (grants 11372239, 11472210 and 11321062).

References

[1] Yang H, Buguin A, Taulemesse J-M, Kaneko K, Méry S, Bergeret A and Keller P 2009 Micron-sized main-chain liquid crystalline elastomer actuators with ultralarge amplitude contractions *J. Am. Chem. Soc.* **131** 15000–4

[2] Naciri J, Srinivasan A, Jeon H, Nikolov N, Keller P and Ratna B R 2003 Nematic elastomer fiber actuator *Macromolecules* **36** 8499–505

[3] Ahir S V, Tajbakhsh A R and Terentjev E M 2006 Self-assembled shape-memory fibers of triblock liquid-crystal polymers *Adv. Funct. Mater.* **16** 556–60

[4] Sánchez-Ferrer A, Fischl T, Stubenrauch M, Wurmus H, Hoffmann M and Finkelmann H 2009 Photo-crosslinked side-chain liquid-crystalline elastomers for microsystems *Macromol. Chem. Phys.* **210** 1671–7

[5] Finkelmann H, Nishikawa E, Pereira G G and Warner M 2001 A new opto-mechanical effect in solids *Phys. Rev. Lett.* **87** 015501

[6] Warner M and Mahadevan L 2004 Photoinduced deformations of beams, plates, and films *Phys. Rev. Lett.* **92** 134302

[7] Jiang H, Li C and Huang X 2013 Actuators based on liquid crystalline elastomer materials *Nanoscale* **5** 5225–40

[8] Yu Y, Nakano M and Ikeda T 2003 Photomechanics: directed bending of a polymer film by light *Nature* **425** 145–145

[9] van Oosten C L, Bastiaansen C W M and Broer D J 2009 Printed artificial cilia from liquid-crystal network actuators modularly driven by light *Nature Mater.* **8** 677–82

[10] Palffy-Muhoray P 2009 Liquid crystals: printed actuators in a flap *Nature Mater.* **8** 614–5

[11] Serak S, Tabiryan N, Vergara R, White T J, Vaia R A and Bunning T J 2010 Liquid crystalline polymer cantilever oscillators fueled by light *Soft Matter* **6** 779–83

[12] Yamada M, Kondo M, Mamiya J-I, Yu Y, Kinoshita M, Barrett C J and Ikeda T 2008 Photomobile polymer materials: towards light-driven plastic motors *Angew. Chem. Int. Ed.* **47** 4986–8

[13] Camacho-Lopez M, Finkelmann H, Palffy-Muhoray P and Shelley M 2004 Fast liquid-crystal elastomer swims into the dark *Nature Mater.* **3** 307–10

[14] Finkelmann H, Kim S T, Muñoz A, Palffy-Muhoray P and Taheri B 2001 Tunable mirrorless lasing in cholesteric liquid crystalline elastomers *Adv. Mater.* **13** 1069–72

[15] Torras N *et al* 2014 Tactile device based on opto-mechanical actuation of liquid crystal elastomers *Sens. Actuators Phys.* **208** 104–12

[16] Ma J and Xuan L 2013 Towards nanoscale molecular switch-based liquid crystal displays *Displays* **34** 293–300

[17] Sánchez-Ferrer A, Fischl T, Stubenrauch M, Albrecht A, Wurmus H, Hoffmann M and Finkelmann H 2011 Liquid-crystalline elastomer microvalve for microfluidics *Adv. Mater.* **23** 4526–30

[18] De Gennes P-G, Hébert M and Kant R 1997 Artificial muscles based on nematic gels *Macromol. Symp.* **113** 39–49

[19] De Gennes P G 1997 A semi-fast artificial muscle *C. R. Acad. Sci. Paris, Ser.* IIB **324** 343–8

[20] Li M-H and Keller P 2006 Artificial muscles based on liquid crystal elastomers *Phil. Trans. R. Soc.* A **364** 2763–77

[21] Li C, Liu Y, Huang X and Jiang H 2012 Direct sun-driven artificial heliotropism for solar energy harvesting based on a photo-thermomechanical liquid-crystal elastomer nanocomposite *Adv. Funct. Mater.* **22** 5166–74

[22] Agrawal A, Luchette P, Palffy-Muhoray P, Biswal S L, Chapman W G and Verduzco R 2012 Surface wrinkling in liquid crystal elastomers *Soft Matter* **8** 7138–42

[23] Agrawal A, Yun T, Pesek S L, Chapman W G and Verduzco R 2014 Shape-responsive liquid crystal elastomer bilayers *Soft Matter* **10** 1411–5

[24] Henann D L, Chester S A and Bertoldi K 2013 Modeling of dielectric elastomers: design of actuators and energy harvesting devices *J. Mech. Phys. Solids* **61** 2047–66

[25] Hon K K, Corbett D and Terentjev E M 2008 Thermal diffusion and bending kinetics in nematic elastomer cantilever *Eur. Phys. J.* E **25** 83–9

[26] Torras N, Zinoviev K E, Marshall J E, Terentjev E M and Esteve J 2011 Bending kinetics of a photo-actuating nematic elastomer cantilever *Appl. Phys. Lett.* **99** 254102
[27] Li M, Lv S and Zhou J 2014 Photo-thermo-mechanically actuated bending and snapping kinetics of liquid crystal elastomer cantilever *Smart Mater. Struct.* **23** 125012
[28] Timoshenko S P and Gere J M 1961 *Theory of Elastic Stability* 2nd edn (New York: McGraw-Hill Book Company Inc.)
[29] He T, Li M and Zhou J 2012 Modeling deformation and contacts of pH sensitive hydrogels for microfluidic flow control *Soft Matter* **8** 3083–9
[30] Huang Z Y, Hong W and Suo Z 2005 Nonlinear analyses of wrinkles in a film bonded to a compliant substrate *J. Mech. Phys. Solids* **53** 2101–18
[31] Mei H, Landis C M and Huang R 2011 Concomitant wrinkling and buckle-delamination of elastic thin films on compliant substrates *Mech. Mater.* **43** 627–42
[32] Stafford C M, Harrison C, Beers K L, Karim A, Amis E J, VanLandingham M R, Kim H-C, Volksen W, Miller R D and Simonyi E E 2004 A buckling-based metrology for measuring the elastic moduli of polymeric thin films *Nature Mater.* **3** 545–50
[33] Zhou J, Hong W, Zhao X, Zhang Z and Suo Z 2008 Propagation of instability in dielectric elastomers *Int. J. Solids Struct.* **45** 3739–50
[34] Guo W, Li M and Zhou J 2013 Modeling programmable deformation of self-folding all-polymer structures with temperature-sensitive hydrogels *Smart Mater. Struct.* **22** 115028